# Lab on a Chip

Check for updates

# Deformability-based microfluidic separation of pancreatic islets from exocrine acinar tissue for transplant applications†

Walter B. Varhue,[a] Linda Langman,[c] Molly Kelly-Goss,[b] Morgan Lataillade,[b] Kenneth L. Brayman,[c] Shayn Peirce-Cottler[b] and Nathan S. Swami (ID) *[a]

The long-term management of type-1 diabetes (T1D) is currently achieved through lifelong exogenous insulin injections. Although there is no cure for T1D, transplantation of pancreatic islets of Langerhans has the potential to restore normal endocrine function *versus* the morbidity of hypoglycemic unawareness that is commonly associated with sudden death among fragile diabetics. However, since endocrine islet tissues form a small proportion of the pancreas, sufficient islet numbers can be reached only by combining islets from multiple organ donors and the transplant plug contains significantly high levels of exocrine acinar tissue, thereby exacerbating immune responses. Hence, lifelong administration of immunosuppressants is required after transplantation, which can stress islet cells. The density gradient method that is currently used to separate islets from acinar tissue causes islets to be sparsely distributed over the centrifuged bins, so that the transplant sample obtained by combining multiple bins also contains significant acinar tissue levels. We show that in comparison to the significant size and density overlaps between the islet and acinar tissue populations post-organ digestion, their deformability overlaps are minimal. This feature is utilized to design a microfluidic separation strategy, wherein tangential flows enable selective deformation of acinar populations towards the bifurcating waste stream and sequential switching of hydrodynamic resistance enables the collection of rigid islets. Using 25 bifurcating daughter channels, a throughput of ~300 islets per hour per device is obtained for enabling islet enrichment from relatively dilute starting levels to purity levels that meet the transplant criteria, as well as to further enhance islet purity from samples following density gradient enrichment. Based on confirmation of viability and functionality of the microfluidic-isolated islets using insulin secretion analysis and an angiogenesis assay, we envision utilizing this strategy to generate small-volume transplant plugs with high islet purity and significantly reduced acinar levels for minimizing immune responses after transplantation.

## Introduction

Type-1 diabetes (T1D) represents the most severe form of the inability to regulate blood glucose levels, wherein the insulin-producing β-cells of pancreatic islets of Langerhans (henceforth called islets) are selectively destroyed by autoimmune re-

[a] *Department of Electrical & Computer Engineering, University of Virginia, Charlottesville, VA 22904, USA. E-mail: nswami@virginia.edu*
[b] *Department of Biomedical Engineering, University of Virginia, Charlottesville, VA 22904, USA*
[c] *Department of Surgery, School of Medicine, University of Virginia, Charlottesville, VA 22904, USA*

† Electronic supplementary information (ESI) available: Video clip of separation; S1: justification of design; S2: volumetric flow rate computation based on threshold bypass pressure measurement; S3: fluidic circuit to minimize flow rate differences across the device footprint; S4: calibration of focusing flows; S5: equivalent circuit model justification and core equations; S6: device operation methodology; S7: details on the density gradient method. See DOI: 10.1039/c7lc00890b

sponses. Currently, long-term management of T1D is achieved through lifelong exogenous insulin administration to synthetically regulate blood glucose levels and achieve energy homeostasis. This therapy can maintain steady glucose levels, but it fails to reverse long-term T1D complications, so diabetics are vulnerable to life-threatening episodes of hypoglycemic and hyperglycemic unawareness. While no long-term cure exists for T1D, transplantation of pancreatic islets has demonstrated the ability to restore normal endocrine function for periods of up to five years.[1,2] However, long-term efficacy of islet transplantation therapy is limited by high costs, exacerbated immune responses due to poor islet purity in transplant sample and complications from lifelong administration of immunosuppressants. This has limited islet transplantation to diabetics vulnerable to glycemic unawareness or those undergoing other transplant procedures.

A primary cause of the exacerbated immune response is the low purity of islets within the packed tissue volume that

is transplanted.[3] The pancreas is largely composed of two tissue types: hormone-producing islets that are specialized aggregates of glucose-regulating endocrine cells (1–2% of the pancreas), embedded into surrounding exocrine acinar tissue that produces digestive enzymes. In the current isolation protocol for the transplant sample from donor pancreas,[1] the mixture of islets and acinar tissue populations post-enzymatic digestion is separated by continuous-flow density gradient (DG) purification. However, due to the insubstantial density difference between islets *versus* acinar populations, as well as the size heterogeneity of islets, the isolated islets are spread over a succession of collected density gradient fractions of varying purity levels. Hence, multiple centrifuged fractions generated from different donor organs must be combined in <10 mL to generate the necessary number of islets for the transplant sample. As a result, the islet transplant sample has a high packed tissue volume with significant acinar tissue levels that cause exacerbated immune responses,[4] lower levels of revascularization[5] and destructive effects due to protease.[6]

We present a microfluidic methodology based on selective deformation of acinar tissue populations *versus* islets for generating transplant samples with high islet purity for potentially alleviating immune responses. The introduction of collagenase into the pancreas through bile duct perfusion to release the tissues destroys the connective acinar tissue structure, while also degrading the outermost component of the skeletal extracellular matrix (ECM) of the islets, which is its basement membrane. For mouse and human islets, it has been shown that the damaged basement membrane of the islets recovers within 24–48 hours after enzymatic digestion,[7] likely due to regrowth of the outer ECM of the islets. This recovery leads to rigid islets that exhibit minimal deformability overlaps with acinar tissue populations, especially in comparison to their substantial size and density overlaps. Hence, separation can be accomplished using tangential flows at an array of microfluidic bifurcations that are designed to deform the acinar tissue towards the bifurcating waste port and collect rigid islet populations downstream of the sample inlet to form transplant plugs with greater islet numbers. Microfluidic methods have been widely applied towards separation of individual cells based on their size,[8] shape,[9] subcellular,[10,11] and deformability[12] characteristics, such as blood cells from healthy *versus* leukaemic patients[13] and oral squamous cells from healthy *versus* cancerous patients,[14] and to distinguish the lineage of stem cells at various differentiation stages.[15] However, while these prior separation methods involved cells with a tight size distribution and of similar shape, the analogous operation of separating multi-cell aggregates based on their deformability characteristics is challenging due to the far broader range of size and shape distributions. Size-based microfluidic filtration has been explored previously for islet collection,[16] but it is prone to clogging and not well-suited for islet *versus* acinar separation due to their size overlaps. Instead, we utilize the minimal deformability overlaps of islet *versus* acinar tissue aggregates

for selective islet isolation, by setting the pressure differential over a series of microfluidic bifurcating junctions to be just sufficient for deforming the acinar tissue through the bifurcating channel to the waste port, while the dynamic adjustment of flow resistance enables the collection of the rigid islets under tangential flow. This microfluidic method enables sufficient selectivity to generate transplant samples with higher islet purity and device scale-up can enhance throughput for isolating sufficient islet numbers. The method maintains islet functionality, as validated by propidium iodide staining, insulin secretion analysis and vascularization assessed using an angiogenesis assay.[17,18]

## Microfluidic device design

### Deformability measurements on cellular aggregates

Techniques such as atomic force microscopy,[19] optical stretching[20] and micropipette aspiration[21] are routinely utilized to measure the deformability of individual cells. However, they are time-consuming, have low throughput, and require expensive equipment and expertise.[22] Furthermore, since the Young's modulus of cellular aggregates is more strongly dependent on intercellular mechanical properties rather than the elasticity of the individual components within the cells,[23] methods based on force application over small areas are likely ill-suited for gauging the deformability of cellular aggregates. In recent years, several high-throughput microfluidic techniques for measuring deformability differences between individual cells have been developed,[22,24] wherein pressure-driven flow across constricting structures is used to induce particle deformation, as measured by means of particle transit time, threshold bypass pressure,[12] induced hydrodynamic or electrical resistance,[25] and particle shape alterations under shear flow.[26] Since these microfluidic methods probe the ability of the particle to deform through a constriction, they can be more easily translated towards a separation application than other characterization methods. However, deformability metrics such as transit time, induced hydrodynamic resistance and induced electrical resistance require a high enough pressure to reliably deform all particle populations. Hence, for the case of multi-cell aggregates that are spread over a far broader range of size and shape distributions than individual cells, the high pressure differentials can damage the aggregates due to the lower yield strength of their intercellular regions *versus* that of the individual component cells.[23] This feature also obviates the use of methods based on particle shape alterations upon repeated or continuous deformation under shear flow. Hence, we choose to measure the threshold bypass pressure, *i.e.* the minimum pressure required to deform the respective aggregate through a constriction, as the metric for deformability differences between islet and acinar tissue populations. While it has lower throughput than continuous deformation methods, this method is preferred, since it limits the applied pressure to the minimum level required to deform the cell aggregate and the measurement only requires a single deformation event.

Constriction designs that cause 100% occlusion for all the tested particles are preferred within prior work on cells,[12] since the pressure differential across the particle rises sensitively with deformability differences between particles. However, this occlusion level cannot be reliably implemented for islets and acinar populations due to their wide size range (60–250 μm) and shape distributions. Instead, in order to maintain a relatively similar pressure differential across the tested particles, we choose constriction designs that create up to 75% occlusion, since the pressure differential across the trapped particle varies linearly within a similar order of magnitude for occlusions up to 75%.[27] In this occlusion regime, while the bypass pressure will vary with aggregate size and shape, the respective deformability differences can be used to compute the required pressure to selectively deform acinar populations *versus* islets (see ESI† sections S1 and S2), thereby achieving micropore separation in spite of the wide and overlapping size distributions. As per Fig. 1, cellular aggregates are individually translated within a batch flow microfluidic device towards the test constriction that is designed to cause no more than 75% particle occlusion. The optimal device was determined to be a channel of 350 μm depth and 400 μm width that contained a lateral constriction of 80 μm, since this represents 80% of the smallest islet diameter in the lateral dimension and 150% of the largest islet diameter in the vertical dimension. This ensures no more than 75% occlusion in the constriction, to create a linearly varying pressure differential across the trapped particle that can be used to compute the required pressure to selectively deform acinar populations *versus* islets.

### Size and deformability-based separation of aggregates

We seek to remove acinar tissue populations that broadly exhibit smaller sizes and higher deformability levels relative to islets, so that the separation strategy causes minimal stress on the collected islets, thereby retaining their viability and angiogenic potential after transplantation. Dead-end microfluidic filtration platforms,[12,16,24] wherein large and rigid particles are selectively trapped under pressure-driven flow across a micro-scale pore, have been widely used for this purpose. However, this method suffers from clogging-induced alterations to the hydrodynamic resistance across pores, thereby increasing the applied pressure over time and resulting in poor selection purity,[28] as well as causing non-reversible adsorption of the particle to the filtration microstructure resulting in sample loss. Cross-flow filtration attempts to alleviate these issues by using a continuous flow tangential to the micro-scale pores, so that large particles can be collected in the direction tangential to the pores that accept small particles.[25,27–29] However, while this method is effective for size-based separation, the tangential flow is unable to maintain a consistent level of deformation on the trapped particle, because the pressure differential is significantly altered upon particle trapping in the constriction region. This is especially problematic with multi-cell aggregates that exhibit wide size and deformability distributions, thereby causing them to require longer time intervals for deformation under a consistent pressure differential. Hence, in order to reduce sample loss and enhance selection purity, we use a two-cycle separation device, wherein two-way piezoelectric switches at each outlet allow for rapid reconfiguration of the hydrodynamic resistance of the flow pathways at a set of bifurcating junctions.

As per Fig. 2a, by using a lower resistance setting at constricting channels of the bifurcating junction *versus* a higher resistance setting at the main outlet, the separation cycle allows deformable acinar particles to pass through to the waste port under pressure-driven flow, while sequentially trapping individual islets at the junction of bifurcating constricting channels. In particular, multi-cell aggregates are focused at the channel wall of the bifurcating junction due to the high-speed focusing flow ($W_a$ determined by the ratio of flow rates of the sample to focusing flow channels) and the hydrodynamic resistance at the main outlet *versus* the bifurcating channel (which depends on $W_S$) is set to enable the selective deformation of aggregates below a desired size range and up to a particular deformability level (as indicated by $W_1$), based on the measured threshold bypass pressure from the previous section. At a critical occlusion level across the array of bifurcating channels, the hydrodynamic flow resistances are switched as per Fig. 2b to enable the tangential flow-based collection cycle, wherein islets that are trapped at the bifurcating junctions are rapidly selected for collection through the main outlet. The arrayed device in Fig. 2c consists of a main channel (400 μm width by 350 μm height) with a series of 25 bifurcating daughter channels (80 μm width by 350 μm height), with each one preceded by a focusing flow channel (100 μm width by 350 μm height). The main channel terminates to an outlet for sample collection, while the bifurcating channels share a common outlet for waste removal. The ratio between the main channel and bifurcating channel resistances is optimized through an equivalent flow
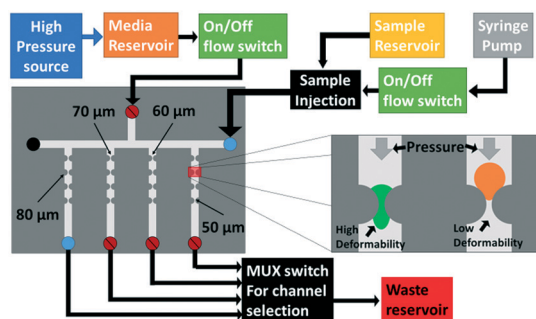


**Fig. 1** Threshold bypass pressure measurements: under successively increasing pressure, more deformable particles (green) pass through the constriction at lower pressure than the particles with lower deformability (orange); the schematic depicts the overall device design and fluidic set-up, using a syringe pump to inject the sample followed by pressure driven flow of individual particles towards the constriction of interest.
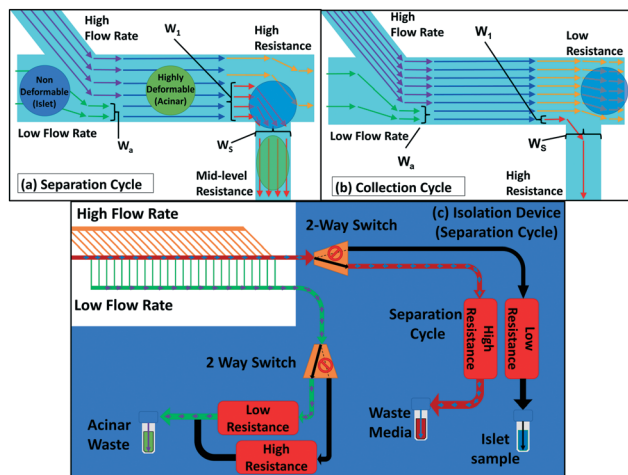
**Fig. 2** Microfluidic tangential flow design with a high-speed focusing flow to place multi-cell aggregates at the channel wall of a bifurcating junction for: (a) the separation cycle wherein a high added resistance at the main outlet is used to direct the flow towards the bifurcating daughter channel for removing smaller and more deformable acinar particles; (b) the collection cycle wherein the flow resistance of the main outlet is lowered *versus* that of the bifurcating channel for periodic collection of rigid islet particles; (c) the device with 25 bifurcating daughter and fluidic connections to enable rapid switching between the separation and collection modes by using a set of flow multiplexers, with pre-programmed time intervals for each cycle that are determined based on occlusion levels due to islets at the bifurcating junctions. Refer to the ESI† for the equivalent fluidic circuit model to adjust the volumetric flow rate (sections S1 and S2) and hydrodynamic resistances (section S3) across the length of the device array, to ensure consistent pressure differentials across each particle trapped at the bifurcating channel, so that they just exceed the threshold bypass pressure for acinar deformation, while being insufficient for islet passage.

circuit model (ESI† section S3) to ensure maintenance of a relatively uniform pressure drop over each channel, independent of distance from the inlet. High-flow rate tangential focusing flows prior to each bifurcating channel are similarly optimized to ensure uniform sample interaction with each bifurcating channel (ESI† section S4). This allows for a rapid, backflow-free method to manipulate flow within the microfluidic device,[30] so that the device can rapidly switch between the separation cycle and the following sample collection cycle to enable the periodic isolation of islets that have been subject to minimal stress.

## Experimental methods

### Pancreas digestion and density gradient purification

The overall sample generation process is presented in Fig. S7.† In order to release the pancreatic islets (Fig. S7a†) and surrounding acinar tissue from the donor pancreas, the collagenase enzyme was introduced through the pancreatic ductal system of a consented research organ donor (Fig. S7b†). After perfusion, the organ was cut into pieces and loaded into a Ricordi digestion chamber containing stainless steel ball bearings to pulverize the tissue, while perfusing with enzyme solution and shaking. Digestion into successively smaller aggregates of endocrine and exocrine tissue was carefully monitored to ensure collection of free and viable islets. Continuous flow to the digestion chamber permits smaller aggregates (<150 μm) to exit through a screen into a collection flask, wherein the enzymatic digestion was quenched with human albumin, followed by cooling and diluting the digest. As a result, the donor organ was reduced to a slurry of islet and acinar aggregates spread over a size range, with an islet purity of 1–2%, thereby requiring additional purification by density gradient separation using a COBE 2991 cell processor to meet the transplantation needs. Herein, a continuous density gradient medium was produced and loaded into the COBE cell processor, so that the density of the medium increases laterally from the centre of the process bag. The tissue sample was loaded into the centre of the process bag, which was then spun at 3000 rpm for 5 minutes. During this time, the centrifugal force separates the digested aggregates along the density gradient, with the denser acinar material moving to the outer regions of the process bag and the lower density islet material remaining towards the centre of the process bag. The contents of the process bag were then separated into 12 fractions of 25 mL. The 12 collected fractions (Fig. 3), as well as the remaining volume in the process bag after the DG separation (usually discarded), were evaluated for islet purity and volume of packed tissue. Collected fractions of similar purity were combined into three different groups of varying purity levels: high (fractions above 80% purity), medium (80–50%), and low (50–30%), while the discarded sample has less than 20% purity. The reported microfluidic enrichment studies were conducted with: (1) a low-purity islet sample (18% purity) isolated from the sample discarded after DG separation and (2) a high-purity islet sample (~60%) generated by combining the collected sample groups to maximize the number of islets, within a total volume <10 mL.

### Microfluidic threshold bypass pressure measurements

Threshold bypass pressure measurements to characterize deformability were carried out using the chip and fluidic
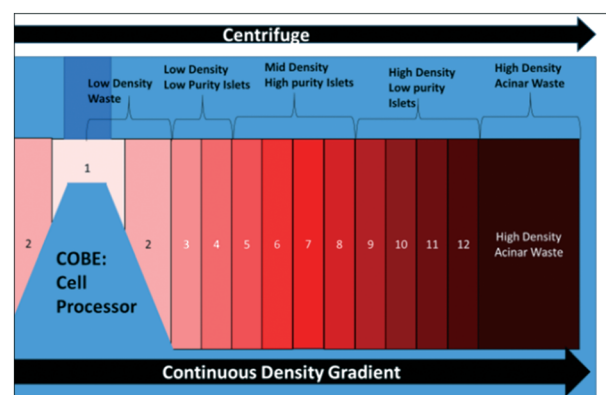


**Fig. 3** Centrifuged fractions from the COBE cell processor for density gradient-based separation for isolation of islet samples for transplantation.

control system shown in Fig. 1. The device is composed of an inverted T-intersection that is used to distribute single aggregates into each of the four individually addressable branching channels (four shown in the schematic) that lead to constrictions of different sizes. After several initial optimizations experiments, we selected the test region composed of a channel with 400 μm width and 350 μm height that has a lateral constriction of 80 μm. To ensure that only a single particle enters the constriction at a time to prevent clogging of the constriction, we used a two-stage batch flow method to select individual sample particles (Fig. S6, ESI†). The sample was injected using a syringe pump to move individual aggregates to the T-intersection. Once the aggregate reached the intersection, the syringe pump was stopped and a pressure-driven flow was applied from the perpendicular channel to carry the aggregate towards the constriction of interest. After the aggregate was moved towards the constriction, the pressure was increased by 25 mbar every 40 seconds, starting at 25 mbar, so that the aggregate deformed through the constriction. This process was recorded using an inverted microscope (Zeiss Observer Z1) to note the pressure at which the tested aggregate passed through the constriction. High pressure was applied to fully remove the deformed aggregate, thereby preventing clogging-induced errors to pressure drop over the device. In the design in Fig. 1, the threshold bypass pressure can be measured simultaneously for four aggregates, which was repeated for a wide range of aggregate sizes that were measured based on their pre-deformed area. For measurements of size and deformability, pure samples of islet and acinar populations isolated from mouse pancreas were measured after 24 hours of enzymatic digestion. Their respective sizes were measured based on pixel area and deformability based on threshold bypass pressure for passage through 80 μm constrictions.

### Microfluidic separation of islets *versus* acinar tissue

The microfluidic enrichment studies from a mixture of islet and acinar aggregates were conducted on the high-purity (~60% islets) and low-purity samples (<20% islets), which were generated, respectively, from the collected and discarded fractions following density gradient separation. As per Fig. 2c, the respective sample was introduced through the main channel inlet and the high-flow rate focusing flow was applied to drive sample aggregates towards bifurcating channels. The multiplexer was programmed for a series of separation and collection modes, with their respective time intervals set based on starting islet levels within the sample (for instance, samples with higher islet levels require successively less separation time in between collection cycles). During the separation mode, the high flow rate directed from the inlet and balancing flows towards the bifurcating channels causes the smaller sized and higher deformability acinar aggregates to be removed through to the waste ports, while also trapping a critical number of rigid islets at the bifurcating junction, with the occlusion detected by flow rate alterations. At a criti-

cal occlusion level, the multiplexer was used to switch the flow resistances to the collection mode, wherein the trapped islets at the bifurcating junctions were carried out through the main outlet port. Following collection, the fluidic control system was reconfigured for the separation mode and this process was repeated multiple times until the entire input sample has been passed through the device. The flow rates of the main carrier and focusing flows required to generate specific pressure drops over the branching channels were numerically calculated using an equivalent fluidic circuit analogy method (ESI† section S3). The flow rates of the focusing flows and the ratio between the main channel and bifurcating channel resistances were chosen to minimize the pressure drop between bifurcating channels in the absence of particles to ensure minimal pressure differences between each bifurcating channel. Based on the sample composition of the respective islet *versus* acinar populations, the time intervals for the separation and collection modes were optimized, such that the separation time between collection cycles is approximately the average time for trapping particles in <50% of the branching channels. Typical values ranged from 21 seconds for input samples with 18% purity to 79 seconds for input samples with 56% purity to enable the continuous collection of a sample with high-purity pancreatic islets.

### Micro-device fabrication

The microfluidic devices utilized in this experiment were fabricated by micro-molding polydimethylsiloxane (PDMS) into a SU-8 negative photoresist master that was patterned on silicon using standard photolithography. The thickness of the patterned photoresist master determines the depth of the microfluidic channel, which was set to 350 μm. To achieve this resist thicknesses, multiple layers of SU-8 3050 were spun onto a 4 inch wafer at 1000 rpm and a modified multistaged soft bake was used. Photolithography was used to pattern the negative photoresist to form a master with a raised inverse structure of 350 μm depth, into which uncured 10:3 PDMS epoxy was poured for micromolding. Following a vacuum degassing step, the mold was allowed to harden overnight on a hot plate. The cured PDMS was then carefully released from the silicon master leaving the microfluidic design molded on its surface. The PDMS mold was then diced into single devices, followed by drilling of design-specific 1/16-th inch inlet and outlet holes with a punch. Following the removal of debris and a low-energy oxygen plasma treatment step, the PDMS channel device was bonded to a glass coverslip.

### Islet viability, insulin secretion and vascularization

All described procedures were conducted in accordance with the policies of the University of Virginia Institutional Animal Care and Use Committee. The functionality of microfluidic-enriched islets was compared to that of pristine islets that were not passed through the device. Viability was quantified

using propidium iodide staining. Insulin secretion was evaluated by standard glucose-stimulated insulin secretion (GSIS) methods, wherein respective islet populations were statically cultured in the glucose concentration range of 20 mM (stimulated) to 2 mM (basal) for an hour. Aliquots of supernatant from each culture were collected for measuring insulin concentrations after 10× dilutions using a mouse ELISA kit (Charles River Laboratories). The stimulation index (SI) was calculated as the ratio of measured insulin concentrations for the stimulated to basal samples. Vascularization of the respective islet populations was studied by transplantation into the corneal micropocket of healthy adult mice, as described within prior protocols into the cornea[18] and the cornea micropocket[17] (ESI† S9). Corneas with transplanted islets were whole-mounted with coverslips on gelatin-coated slides using a 50:50 glycerol/PBS solution. Digital images of the corneal and islet vasculature were acquired using confocal microscopy (Nikon Instruments Incorporated, Melville, NY; Model TE200-E2; 10×, 20× and 60× objectives); full-thickness $z$-stack (2 μm steps) volume renders were used to capture the entire thickness of the corneal and islet vascular networks in each field of view.

## Results and discussion

### Transplant sample from the density gradient method

The limitations on % islet purity in transplant samples generated by the density gradient (DG) method are explored in Fig. 4, based on 22 islet isolation procedures using human donor research organs (details in ESI† S8). Herein, while the islets are localized within the collected fractions of mid-level density and the acinar tissues are mostly localized in the uncollected discarded waste, there is a considerable degree of overlap between the two populations that leads to significant acinar contamination within the collected sample. Due the low islet numbers and the low total packed tissue volume

in the collected fractions (those of purity >30%), these fractions must be combined to generate the net transplant sample. As a result, the islet transplant sample after DG isolation contains significant acinar tissue levels (up to 40%), while the discarded bins (i.e. those with <30% islet purity) due to their high volume represent a 15% loss in the overall islets from the donor organ, resulting in ~85% collection efficiency of islets.

### Deformability overlaps for islets versus acinar particles

In order to utilize deformability as the basis for separation of islets from acinar tissue populations, we compare the overlaps in the distribution of their size and deformability. The latter is determined based on threshold bypass pressure for passage through 80 μm constrictions, as per the device in Fig. 1. The data in ESI† Fig. S9 shows a successive increase in threshold bypass pressure of islets, onward from day 2 (pancreas digestion occurs on day 1) to day 5, followed by gradual loss of islet viability, whereas threshold bypass pressure for acinar tissue remains unchanged. This strongly suggests regrowth of the damaged basement membrane of the islets in the 24–48 hour period after enzymatic digestion of pancreas, causing islets to become more rigid versus acinar tissues. Hence, the samples within this work are standardized to those obtained after the 24–48 hour period (just after day 2) wherein islets retain their highest % viability and are significantly more rigid than acinar populations. As per Fig. 5a, while the average sizes of the islets are significantly larger than those of acinar tissue populations, there is a considerable degree of overlap, which is somewhat consistent with the respective histograms of the DG method (Fig. 4) that show poor separation, likely due to density overlaps. On the other hand, Fig. 5b shows a relatively small degree of deformability overlap for islet versus acinar tissue populations, since just 9% of the islet population and 19% of the acinar population have deformabilities corresponding to threshold bypass pressure within the overlap region (for ~100 measured aggregates). These overlaps become insignificant at applied pressure differentials beyond 150 mbar (inset of Fig. 5b shows the deformation of islets for passage through 80 μm constrictions at a threshold bypass pressure of 200 mbar). The plot of aggregate area versus threshold bypass pressure in Fig. 5c indicates that while the deformability of islets rises linearly with their area, the same is not apparent with acinar populations. This uniformity in trend of islet stiffness suggests the continuing role of the extracellular matrix (ECM), whereas acinar tissues show a heterogeneous deformability distribution, likely due to their degraded ECM. The deformability overlap of islet versus acinar populations in Fig. 5b is used to quantify the possible separation purity and collection efficiency numbers within a separation device, by computing the anticipated islet purity and sample loss using applied pressure levels up to 200 mbar, for starting samples: 60% purity within Fig. 6a (as obtained after DG separation), 50% purity within Fig. 6b (an intermediate level)
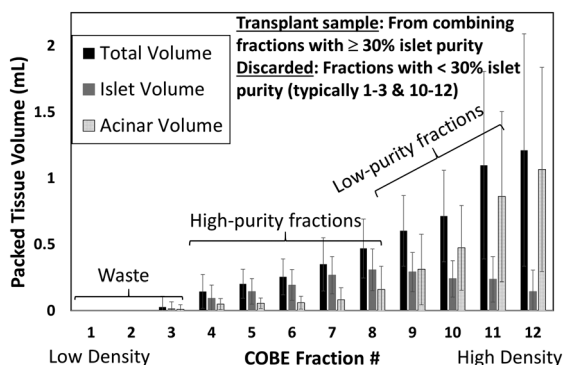


Fig. 4 Packed tissue volume (mL) of islets versus acinar tissue within the total volume collected at each centrifuged fraction from the COBE system. Typically, fractions 4–8 need to be combined to generate the transplant plug, while fractions 9–12 must be discarded due to high levels of acinar tissue contamination. Example raw data is shown in Fig. S8C (ESI†) classified within sample bins: high purity (>80%), medium purity (50–80%), low purity (30–50%) and waste samples (<30% purity).
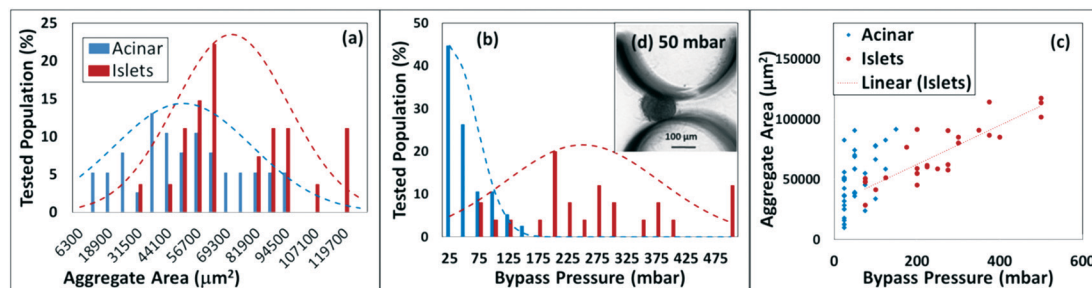
**Fig. 5** (a) Size overlaps of acinar *versus* islet particles are shown as a histogram of the respective particle area; (b) deformability overlaps of acinar *versus* islet particles are shown as a histogram of the threshold bypass pressure (mbar) for passage of the respective particles; (c) scatter plot of the area of the respective aggregate (islet or acinar) against their threshold bypass pressure shows that a clear linear relationship is apparent only for the islets; (d) example threshold bypass pressure measurement for a typical islet at 50 mbar applied pressure through an 80 μm constriction (islet and acinar sample after day 2 of pancreas digestion).
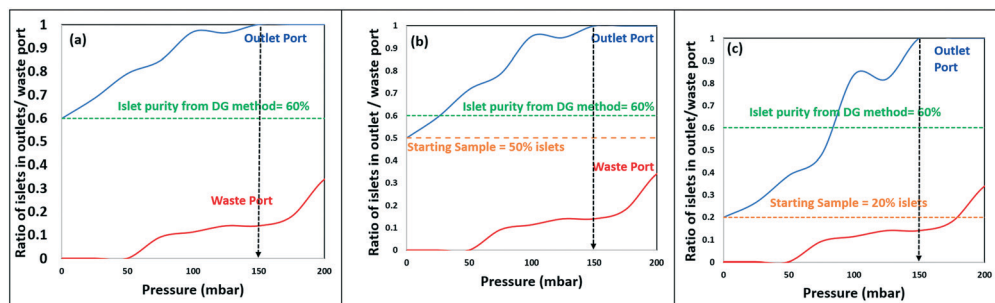


**Fig. 6** Computed ratio of islet levels obtained in the outlet (separation purity) and waste ports (sample loss) using the separation device (Fig. 2c) at pressure differentials up to 200 mbar, for starting samples: (a) 60% islets (after DG separation); (b) 50% islets (intermediate); (c) 20% islets (discarded from the DG method).

and 15% purity within Fig. 6c (discarded residue from DG separation). These plots suggest that a pressure differential of 50 mbar can enrich islets with near-zero sample loss from 60% to 80% (Fig. 6a), from 50% to 70% (Fig. 6b), and from 15% to 30% levels (Fig. 6c). If sample losses of 10–15% can be tolerated, an islet sample with 95% purity can be obtained from the starting sample after DG separation (60% purity) using a 100 mbar pressure differential and islet samples with near 100% purity can be obtained from all three starting samples (60%, 50% and 15%) using a 150 mbar differential.

**Microfluidic separation of islet *versus* acinar particles**

The microfluidic device in Fig. 2c was applied as per the separation methodology described previously to quantify the degree of islet enrichment for two different starting islet samples: 18% and 56% purity. Based on an equivalent fluidic circuit model, the volumetric flow rate (ESI† S1 & S2) and hydrodynamic resistances (ESI† S3) were adjusted across the length of the device array, to ensure consistent pressure differentials across each particle trapped at the bifurcating channel, so that these values just exceed the threshold bypass pressure for acinar deformation, while being insufficient for islet passage. For the islet sample with 18% purity, the separation mode was operated for 79 seconds followed by operation in the collection mode for 10 seconds, while for the sam-

ple with 56% purity, the separation mode was operated for 21 seconds followed by operation in the collection mode for 10 seconds. As per Fig. 7, for sample entry and placement at bifurcating points through the array of focusing flows, islet populations are trapped at the bifurcating points (Fig. 7A and C) during the separation mode, while acinar particles are removed by deformation from the bifurcating point through to the waste port (Fig. 7B and D). It is clear that the trapped islets at a given bifurcating point do not hinder the flow of acinar particles to the successive bifurcating points, so the trapped islets (Fig. 7E) can then be isolated under the collection mode. Table 1 shows the key figures of merit on measured islet purity and sample loss for two starting samples (18% and 56% purity) using the device in Fig. 2c, in comparison to the respective computed numbers, based on the deformability overlap in Fig. 5b. The relatively good correlation between the measured and computed parameters confirms the role of deformability-based differences within the observed separation.

These results demonstrate that the microfluidic deformability-based separation methodology can enable enrichment of islets from samples with a wide distribution of starting islet purities, including samples obtained after DG separation (~60% purity) and the rather dilute samples discarded by the DG separation method (<20% purity). Under operation within the separation mode with a flow rate of
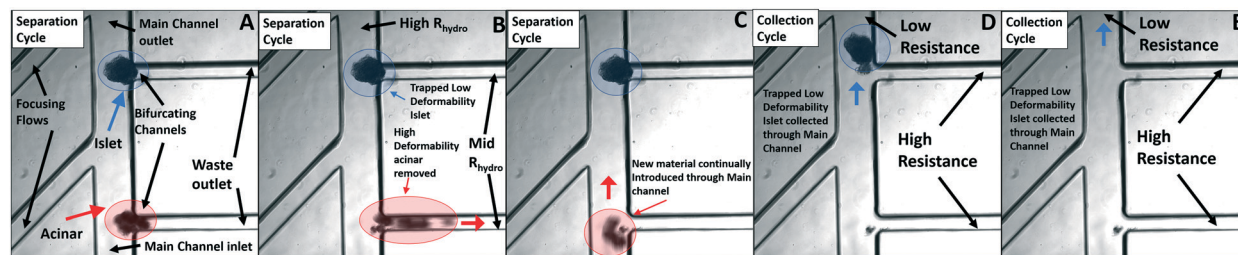
**Fig. 7** (See video clip) The microfluidic device in Fig. 2c (main channel flow from bottom to top, with focusing flows on the left side and bifurcating channels on the right side) is applied under the separation mode with a flow rate of 75 $\mu$L h$^{-1}$ through the bifurcating daughter channels (analogous to the 100 mbar applied pressure in the single channel as per the analysis in section 2 of the ESI†) to remove acinar populations (red circles) from the bifurcating points towards the waste port (A–C), while the collection mode (switch outlet resistance) is used to isolate the trapped islets at bifurcating points (blue circles) towards the main outlet port (D and E).

75 $\mu$L h$^{-1}$ through the bifurcating daughter channels (analogous to the 100 mbar applied pressure in the single channel as per the detailed analysis in section 2 of the ESI†), islets are collected at a rate of 6 islets per minute, when a typical input sample from the DG method with 56% islet purity is used. The time between the separation and collection cycles is determined by the number of daughter channels. Typically, the device is run such that 50% of the daughter channels would contain a trapped islet before collection. For the current device with 25 daughter channels that covers a footprint of 8 mm (width) × 15 mm (length) × 0.1 mm (depth), the separation cycle is run for 2.5 minutes, followed by 10 seconds of collection cycle, enabling collection of ∼300 islets per h per device. In order to reach the necessary islet numbers to meet the transplantation needs, a number of devices would be run in parallel. For instance, the collection of a sample with 100 000 islets of >90% sample purity would require 342 devices that cover a footprint of 9″ × 9″. Since this footprint can be further condensed utilizing multilayer fabrication or 3D printing methods, we assess that the reported methodology is scalable.

## Viability and functionality of microfluidic-sorted islets

Based on minor differences in % pixels with intensity ≥ twofold intensity above background after propidium iodide staining (this intensity threshold most accurately represented non-viable islets) in Fig. 8(i) for pristine unsorted islets *versus*

microfluidic-sorted islets, we infer that the islets isolated by this microfluidic method retain their viability. The islets recovered from the device were studied for their ability to vascularize within the corneas of mice. As seen in Fig. 8a, the mouse cornea is a clear, avascular tissue available for exogenous islet transplantation. By placing an islet in the corneal epithelial layer, close to the limbus, we are able to observe the viability and vascularity of the islets (Fig. 8b–d and f–h). Fig. 8e shows a 27-gauge needle being used to place islets into the cornea. After transplantation, both sorted (Fig. 8b–d) and unsorted (Fig. 8f–h) islets remain viable in the tissue and their vasculature is able to incorporate with the capillaries surrounding the mouse cornea. Fig. 8c and f show sorted and unsorted pristine pancreatic islets seven days after being placed into the cornea, respectively. The respective islets are viable and incorporated into the local vasculature, as shown by capillaries labeled for an endothelial cell marker, CD31, in Fig. 8c and g. The depth of the vasculature in the tissue (Fig. 8d and h) is indicated calorimetrically, where cooler-colored (blue-cyan) blood vessels are further away from the warmer-colored (red-orange) vessels. Based on this, we can see vessels that travel from the limbus (in red) into the islet (in blue), indicating that the islets have been successfully vascularized and remain viable in the tissue.

To enable quantitative comparisons of vascularization, three islets per cornea were surgically implanted into the left and right corneas of three anesthetized mice on day 0, with one cornea receiving microfluidic-sorted islets and the contralateral cornea receiving pristine islets (randomized for each mouse). The metric of vessel density per mm$^2$ reports the raw integrated density (sum of pixel intensities within the region of interest) divided by the area of the region of interest, and quantifies the percent area taken up by vascularization in the islets. At day 28, vessel density per mm$^2$ was quantified to be 15.3 ± 6.8 for the sorted samples and 13.08 ± 6.7 for the pristine islets. This data suggests that the microfluidic-sorting step has not significantly altered the ability of the sorted islets to vascularize *versus* the pristine unsorted islets, since the differences in measured vessel density per mm$^2$ for these two groups is not statistically different ($p < 0.05$, paired *t*-test). Finally, insulin secretion measured by the GSIS assay on 10 islets per group shows average

**Table 1** Comparison of transplant samples after microfluidic separation of islets from acinar tissue populations (device in Fig. 2c) for two starting islet levels. The % levels are based on measurements *versus* prediction from deformability distribution (Fig. 5b). Note that the measured loss is less than predicted due to deformation time-induced discrepancy. Throughput: ∼300 islets per h per device

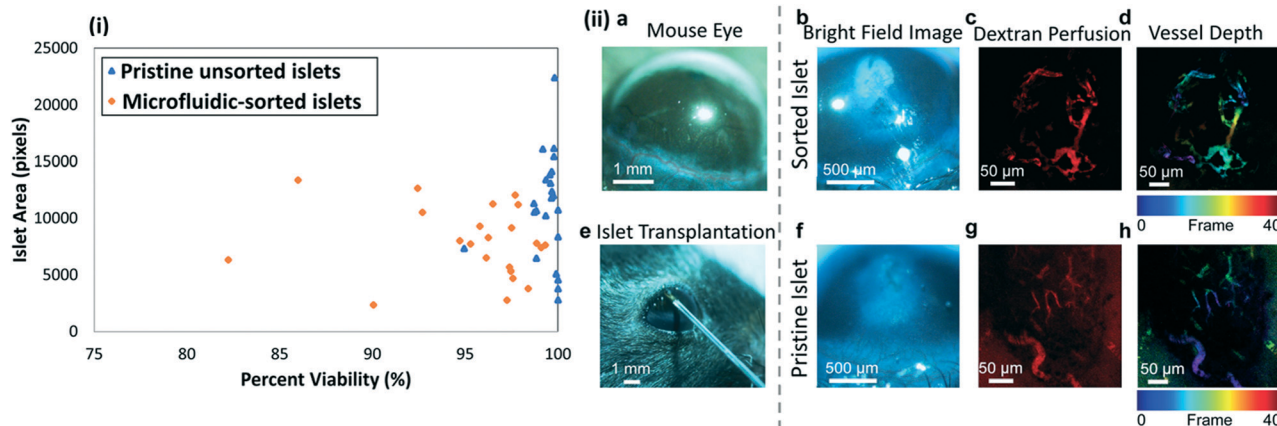| Figure of merit | Sample 1 | | Sample 2 | |
|---|---|---|---|---|
| | Measured | Predicted | Measured | Predicted |
| Starting islet purity | 18% | 18% | 56% | 56% |
| Final islet purity | 62% | 82% | 88% | 96% |
| Acinar removed | 87% | 95% | 83% | 98% |
| Loss in islets | 5% | 11% | 0% | 11% |
| Volume reduction | 62% | 78% | 37% | 42% |

**Fig. 8** (i) Percent viability of pristine (unsorted) islets *versus* microfluidic-sorted islets based on % pixels with 2-fold intensity above background (non-viable tissue) after PI staining; (ii) islet vascularization based on angiogenesis assay. (a and e) Sorted and pristine pancreatic islets were placed into the mouse cornea using the corneal micropocket assay, (b and f) where they remained viable for at least seven days. (c and d and g and h) Both sorted and pristine islets incorporated their vasculature into the nearby capillary network, as indicated by (c and g) capillaries labelled with the endothelial cell marker CD31, and (d and h) were observed going from the limbus vessels (red-orange) into the pancreatic islet (blue-cyan) in the corneal epithelium 28 days after transplantation with the respective islet.

stimulation index (SI) values of 1.85 ± 0.19 for the microfluidic-sorted islets and 1.54 ± 0.26 for the pristine islets, suggesting no significant influence of the sorting procedure on the insulin secretion levels of islets.

## Conclusions

The isolation of pancreatic islets using the density gradient-based separation method is shown to result in a transplant plug with 60% or less islet purity, due to the wide distribution of islets across the centrifuged sample bins, which likely occurs due to the density overlap between islets and a significant portion of acinar particles. Hence, due to the relatively sparse islet levels in a given bin, there is a need to combine samples from multiple bins and/or donor organs, thereby causing significant acinar tissue levels within the final transplant plug that exacerbates immune rejection. We show that the minimal overlap in deformability levels of islet *versus* acinar tissue populations can enable selective isolation of islets *versus* acinar tissue, by adjusting the pressure drops to enable the deformation of acinar populations through bifurcating junctions within a microfluidic device, while collecting islets under tangential flow. We design a two-cycle microfluidic device wherein the hydrodynamic flow resistance towards the outlet is switched from a "high" level within a separation mode for removal of deformable acinar populations to a "low" level for isolation of rigid islets trapped at bifurcating points within a collection mode. This separation device is capable of enriching islets from dilute levels (18%) up to purity levels that meet transplant criteria, as well as for enriching islet purity levels beyond the 60% levels, for samples obtained after density gradient-based separation. Finally, purified islets isolated by the microfluidic method are shown to be viable and functional, based on insulin secretion analysis and vascularization that is assessed using an angiogenesis assay.

## Conflicts of interest

There are no conflicts to declare.

## Acknowledgements

## Notes and references

1 C. Ricordi and T. B. Strom, Clinical islet transplantation: advances and immunological challenges, *Nat. Rev. Immunol.*, 2004, 4(4), 259–268.

2 R. M. Langer, Islet Transplantation: Lessons Learned Since the Edmonton Breakthrough, *Transplant. Proc.*, 2010, 42(5), 1421–1424.

3 H. Ichii, A. Pileggi, R. D. Molano, D. A. Baidal, A. Khan, Y. Kuroda, L. Inverardi, J. A. Goss, R. Alejandro and C. Ricordi, Rescue purification maximizes the use of human islet preparations for transplantation, *Am. J. Transplant.*, 2005, 5(1), 21–30.

4 D. W. R. Gray, R. Sutton, P. Mcshane, M. Peters and P. J. Morris, Exocrine Contamination Impairs Implantation of Pancreatic-Islets Transplanted beneath the Kidney Capsule, *J. Surg. Res.*, 1988, 45(5), 432–442.

5 M. Heuser, B. Wolf, B. Vollmar and M. D. Menger, Exocrine contamination of isolated islets of langerhans deteriorates the process of revascularization after free transplantation, *Transplantation*, 2000, 69(5), 756–761.

6 G. Loganathan, R. K. Dawra, S. Pugazhenthi, Z. Guo, S. M. Soltani, A. Wiseman and M. A. Sanders, Insulin degradation by acinar-cell proteases creates a dysfunctional environment for human islets before/after transplantation: Benefits of alpha-1 antitrypsin treatment, *Transplantation*, 2011, 92(11), 1222.

7 R. N. Wang, S. Paraskevas and L. Rosenberg, Characterization of integrin expression in islets isolated from hamster, canine, porcine, and human pancreas, *J. Histochem. Cytochem.*, 1999, **47**(4), 499–506.

8 M. Yamada, M. Nakashima and M. Seki, Pinched flow fractionation: Continuous size separation of particles utilizing a laminar flow profile in a pinched microchannel, *Anal. Chem.*, 2004, **76**(18), 5465–5471.

9 M. L. Jiang, K. Budzan and G. Drazer, Fractionation by shape in deterministic lateral displacement microfluidic devices, *Microfluid. Nanofluid.*, 2015, **19**(2), 427–434.

10 Y.-H. Su, A. Rohani, C. A. Warren and N. S. Swami, Tracking Inhibitory alterations during interstrain clostridium difficile interactions by monitoring cell envelope capacitance, *ACS Infect. Dis.*, 2016, **2**(8), 544–551.

11 A. Rohani, J. H. Moore, J. A. Kashatus, H. Sesaki, D. F. Kashatus and N. S. Swami, Label-free quantification of intracellular mitochondrial dynamics using dielectrophoresis, *Anal. Chem.*, 2017, **89**(11), 5757–5764.

12 M. E. Myrand-Lapierre, X. Y. Deng, R. R. Ang, K. Matthews, A. T. Santoso and H. S. Ma, Multiplexed fluidic plunger mechanism for the measurement of red blood cell deformability, *Lab Chip*, 2015, **15**(1), 159–167.

13 J. M. Jackson, J. B. Taylor, M. A. Witek, S. A. Hunsucker, J. P. Waugh, Y. Fedoriw, T. C. Shea, S. A. Soper and P. M. Armistead, Microfluidics for the detection of minimal residual disease in acute myeloid leukemia patients using circulating leukemic cells selected from blood, *Analyst*, 2016, **141**(2), 640–651.

14 S. E. Weigum, P. N. Floriano, N. Christodoulides and J. T. McDevitt, Cell-based sensor for analysis of EGFR biomarker expression in oral cancer, *Lab Chip*, 2007, 7(8), 995–1003.

15 H. W. Wu, C. C. Lin and G. B. Lee, Stem cells in microfluidics, *Biomicrofluidics*, 2011, **5**(1), 013401.

16 K.-H. Nam, W. Yong, T. Harvat, A. Adewola, S. Wang, J. Oberholzer and D. T. Eddington, Size-based separation and collection of mouse pancreatic islets for functional analysis, *Biomed. Microdevices*, 2010, **12**(5), 865–874.

17 M. S. Rogers, A. E. Birsner and R. J. D'amato, The mouse cornea micropocket angiogenesis assay, *Nat. Protoc.*, 2007, **2**(10), 2545–2550.

18 M. Paschen, T. Moede, B. Leibiger, S. Jacob, G. Bryzgalova, I. B. Leibiger and P.-O. Berggren, Non-invasive cell type selective in vivo monitoring of insulin resistance dynamics, *Sci. Rep.*, 2016, **6**, 21448.

19 M. Fornal, M. Lekka, G. Pyka-Fosciak, K. Lebed, T. Grodzicki, B. Wizner and J. Styczen, Erythrocyte stiffness in diabetes mellitus studied with atomic force microscope, *Clin. Hemorheol. Microcirc.*, 2006, **35**(1–2), 273–276.

20 J. Guck, R. Ananthakrishnan, H. Mahmood, T. J. Moon, C. C. Cunningham and J. Kas, The optical stretcher: A novel laser tool to micromanipulate cells, *Biophys. J.*, 2001, **81**(2), 767–784.

21 R. M. Hochmuth, Micropipette aspiration of living cells, *J. Biomech.*, 2000, **33**(1), 15–22.

22 Y. Zheng, J. Nguyen, Y. Wei and Y. Sun, Recent advances in microfluidic techniques for single-cell biophysical characterization, *Lab Chip*, 2013, **13**(13), 2464–2483.

23 P. R. Baraniak, M. T. Cooke, R. Saeed, M. A. Kinney, K. M. Fridley and T. C. McDevitt, Stiffening of human mesenchymal stem cell spheroid microenvironments induced by incorporation of gelatin microparticles, *J. Mech. Behav. Biomed. Mater.*, 2012, **11**, 63–71.

24 D. Qi, D. J. Hoelzle and A. C. Rowat, Probing single cells using flow in microfluidic devices, *Eur. Phys. J.: Spec. Top.*, 2012, **204**(1), 85–101.

25 Y. Zheng, J. Nguyen, C. Wang and Y. Sun, Electrical measurement of red blood cell deformability on a microfluidic device, *Lab Chip*, 2013, **13**(16), 3275–3283.

26 O. Otto, P. Rosendahl, A. Mietke, S. Golfier, C. Herold, D. Klaue, S. Girardo, S. Pagliara, A. Ekpenyong, A. Jacobi, M. Wobus, N. Topfner, U. F. Keyser, J. Mansfeld, E. Fischer-Friedrich and J. Guck, Real-time deformability cytometry: on-the-fly cell mechanical phenotyping, *Nat. Methods*, 2015, **12**(3), 199–202.

27 J. S. Kuo, Y. X. Zhao, P. G. Schiro, L. Y. Ng, D. S. W. Lim, J. P. Shelby and D. T. Chiu, Deformability considerations in filtration of biological cells, *Lab Chip*, 2010, **10**(7), 837–842.

28 S. M. McFaul, B. K. Lin and H. S. Ma, Cell separation based on size and deformability using microfluidic funnel ratchets, *Lab Chip*, 2012, **12**(13), 2369–2376.

29 X. Chen, D. F. Cui, C. C. Liu, H. Li and Z. X. Geng, Microfluidic cell separation chips based on crossflow filtration, *Chem. J. Chinese U.*, 2007, **28**(1), 59–61.

30 A. Rohani, B. J. Sanghavi, A. Salahi, K.-T. Liao, C.-F. Chou and N. S. Swami, Frequency-selective electrokinetic enrichment of biomolecules in physiological media based on electrical double-layer polarization, *Nanoscale*, 2017, **9**, 12124–12131.